



# Room temperature synthesis and enhanced photocatalytic property of CeO<sub>2</sub>/ZnO heterostructures

Chao Wang<sup>1</sup> · Huiqing Fan<sup>1</sup> · Xiaohu Ren<sup>1</sup> · Jiawen Fang<sup>1</sup>

Received: 4 May 2017 / Accepted: 29 December 2017 / Published online: 9 January 2018  
© Springer-Verlag GmbH Germany, part of Springer Nature 2018

## Abstract

To achieve better photocatalytic performance, we proposed a facile solid-state reaction method to produce CeO<sub>2</sub>/ZnO heterostructures. Ceria and zinc oxide were synthesized simultaneously by thoroughly grinding the mixture of zinc acetate dihydrate, cerium nitrate hexahydrate and sodium hydroxide. The morphology of the as-prepared heterostructures varies dramatically as different amount of ceria was introduced in the composition. The photocatalytic performance of CeO<sub>2</sub>/ZnO heterojunctions was 4.6 times higher than that of pure ZnO. The enhanced photocatalytic activity could be ascribed to that more electrons and holes could transport to the surface of catalysts and react with the pollution due to the extended light-responsive range, accelerated migration, increased specific surface area and suppressed recombination of photogenerated carriers.

## 1 Introduction

Oxide semiconductor photocatalysis is an environmentally friendly approach toward solving the energy shortage and realizing environmental remediation issues [1–3]. As a widely used metal oxide semiconductor, zinc oxide (ZnO) is regarded as an ideal candidate for gas sensing [4], dye-sensitized solar cells [5] and photocatalysts [6]. Due to its unique optical and electronic properties, ZnO has become a potential photocatalyst for industrialized application. However, the practical use of ZnO is limited for its wide band gap and rapid recombination of charge carriers [7]. Several means have been used to improve the photocatalytic property of ZnO, such as doping with foreign atoms [8–11], defect control [12–14], deposition of noble metals [15–17] and formation of heterostructures with semiconductors [18–21] and carbonaceous materials [22, 23]. Among all these methods, formation of composite photocatalysts has been considered the most efficient strategy to improve the photocatalytic property of ZnO. Han and co-workers prepared a ternary CdS-decorated 1D ZnO nanorods–2D graphene hybrid by a simple, low-temperature synthesis approach [24]. The

as-prepared nanocomposite showed greatly enhanced photocatalytic performance in reduction of 4-nitroaniline to *p*-phenylenediamine compared with both ZnO and CdS-decorated ZnO.

Ceria (CeO<sub>2</sub>) has attracted much attention due to its applications in catalysis and chemical material [25, 26]. The smaller band gap of CeO<sub>2</sub> promises its broader spectral responsive range than that of ZnO. For better photocatalytic performance, extensive researches have been developed to prepare CeO<sub>2</sub>/ZnO heterostructures by different approaches. Li et al. prepared CeO<sub>2</sub>/ZnO nanofibers via electrospinning technique [27]. The photocatalytic activity of CeO<sub>2</sub>/ZnO nanofiber is 2.1 times higher than that of pure ZnO. Faisal et al. reported CeO<sub>2</sub>/ZnO nanoparticles which showed excellent performance in photodegradation of methylene blue [28]. The results indicate that forming heterojunctions with CeO<sub>2</sub> could enhance the optical absorption property of ZnO and thus improve the photocatalytic performance. However, all these methods involved complex procedures and rigorous experimental conditions, such as high temperature and a long processing time, and the products obtained often showed poor photocatalytic activity. Therefore, it is extremely necessary to develop simple and reliable synthetic methods for heterojunctions with excellent photocatalytic properties. Herein, we suggested a facile solid-state reaction method which is simple, fast and economic, and does not require high-temperature process and complicated setups. What's more, the heterostructures prepared via solid-state

✉ Huiqing Fan  
hqfan3@163.com

<sup>1</sup> State Key Laboratory of Solidification Processing, School of Materials Science and Engineering, Northwestern Polytechnical University, Xi'an 710072, China

reaction method show good photocatalytic activity for degradation of Rhodamine B (RhB).

## 2 Experimental section

### 2.1 Materials and synthesis of samples

All reagents were analytically pure and used without further purification. In a typical procedure, 0.219 g  $\text{Zn}(\text{CH}_3\text{COO})_2 \cdot 2\text{H}_2\text{O}$  were blended with different amount of  $\text{Ce}(\text{NO}_3)_3 \cdot 6\text{H}_2\text{O}$  in an agate mortar and ground for 20 min at room temperature. Then, 0.32 g NaOH was added to the mixture and ground for another 60 min. After that, the paste was washed with distilled water and absolute ethanol in turn for three times. Finally, the products were obtained after drying at 60 °C for 8 h. The illustration for synthesis of  $\text{CeO}_2/\text{ZnO}$  heterostructures is shown in Fig. 1. The samples with 0, 2, 5 and 10% (molar ratios)  $\text{CeO}_2$  were marked as ZnO, 2%  $\text{CeO}_2/\text{ZnO}$ , 5%  $\text{CeO}_2/\text{ZnO}$  and 10%  $\text{CeO}_2/\text{ZnO}$ , respectively.

### 2.2 Characterization

The phase structure of the  $\text{CeO}_2/\text{ZnO}$  heterostructures was examined by X-ray diffraction (XRD; X'pert, Philips, Eindhoven, The Netherlands). The morphology was investigated using field emission scanning electron microscopy (FE-SEM; JSM-6701F, JEOL, Tokyo, Japan) and transmission electron microscopy (TEM; Tecnai F30G2, FEI, Hillsboro, OR, USA). The X-ray photoelectron spectroscopy (XPS) measurements were performed on a spectrometer (VGES-CALAB220i-XL, Thermo Scientific, Waltham, MA, USA). Their light absorption abilities were analyzed in the range of 300–700 nm by the UV–Vis spectrometer (U-3900H, Hitachi, Tokyo, Japan), during which  $\text{BaSO}_4$  was employed as the internal reflectance standard. The photoluminescence (PL) spectrum was recorded with a fluorescence spectrophotometer (F-4600, Hitachi, Tokyo, Japan) excited by an

incident light of 325 nm. The Brunauer–Emmett–Teller (BET) surface area was determined by nitrogen adsorption–desorption isotherm measurements (VSOB-2800 P, Gold APP Corp., Beijing, China) at 77 K. Electrochemical impedance spectrometer (EIS; CHI660E, Chenhua, Shanghai, China) experiments were performed with a conventional three-electrode cell, using a Pt plate as the counter electrode and an Ag/AgCl electrode (3 M KCl) as the reference electrode.

### 2.3 Evaluation of photocatalytic activity

The photocatalytic activity of  $\text{CeO}_2/\text{ZnO}$  heterostructures was evaluated by photodegradation of RhB under simulated solar light. 30 mg of the catalyst was dispersed in 30 mL RhB aqueous solution with a concentration of 10 mg/L and stirred for 30 min in dark to establish adsorption/deposition equilibrium. Then the suspension was exposed to a Xe lamp (500 W, 300–800 nm) for photocatalytic reaction under vigorous stirring. The suspension was taken out every 15 min and centrifuged. Change in the concentration of dye was analyzed by UV–visible spectrophotometer (UV-2450, Shimadzu, Kyoto, Japan).

## 3 Results and discussion

To analyze the phase structure of the products, XRD patterns of all samples are shown in Fig. 2a. All peaks of ZnO are in good agreement with the standard spectra (JCPDS no. 36-1451). The peaks located at 31.8°, 34.5°, 36.3°, 47.6°, 56.6°, 62.9°, 66.4°, 68.0° and 69.1° are ascribed to the (100), (002), (101), (102), (110), (103), (200), (112) and (201) lattice plane of ZnO. The peak located at 28.55° corresponding to (111) crystal plane of fluorite  $\text{CeO}_2$  (JCPDS no. 34-0394) is also observed in the insert of Fig. 2a. The calculated grain size of ZnO and  $\text{CeO}_2$  in each sample is listed in Table 1. The results indicate that introduction of  $\text{CeO}_2$  in

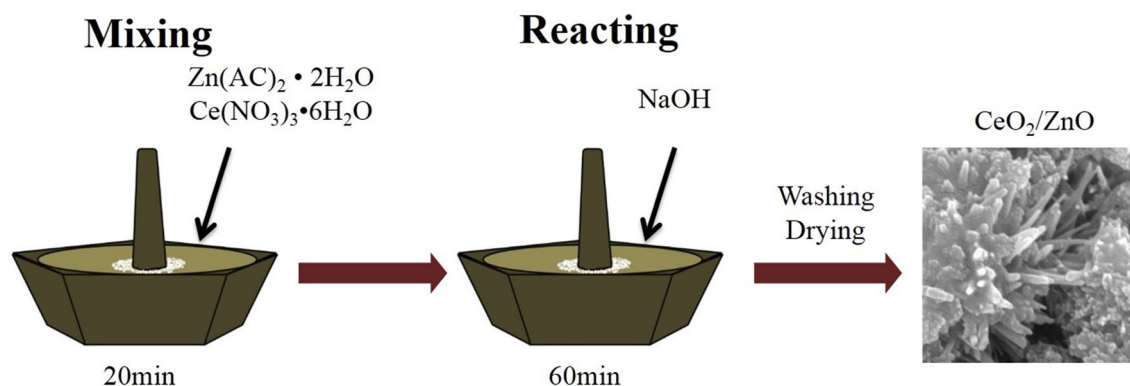
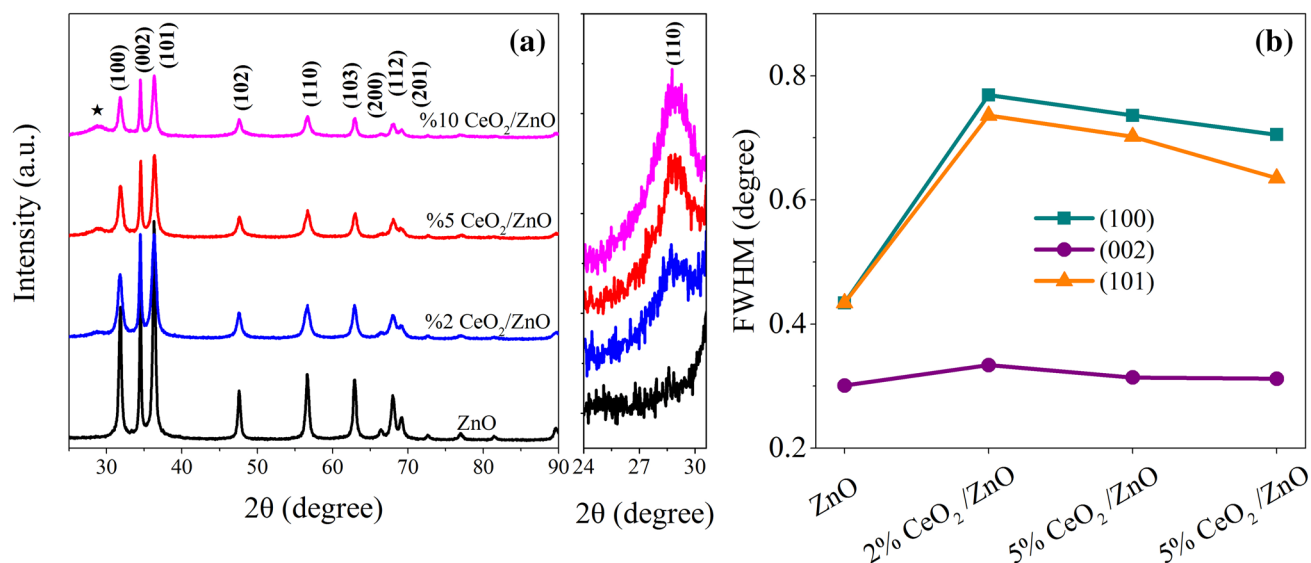


Fig. 1 Preparation procedure of  $\text{CeO}_2/\text{ZnO}$  heterostructures



**Fig. 2** **a** XRD patterns of CeO<sub>2</sub>/ZnO heterostructures with different amount of CeO<sub>2</sub>, the insert is the magnification from 24° to 32°, **b** FWHM of (100), (002) and (101) peak for the as-prepared samples

**Table 1** Calculated grain size of ZnO and CeO<sub>2</sub> in the as-prepared ZnO and CeO<sub>2</sub>/ZnO heterostructures

Sample	ZnO		2% CeO <sub>2</sub> /ZnO		5% CeO <sub>2</sub> /ZnO		10% CeO <sub>2</sub> /ZnO	
Component	ZnO	CeO <sub>2</sub>	ZnO	CeO <sub>2</sub>	ZnO	CeO <sub>2</sub>	ZnO	CeO <sub>2</sub>
Grain size (nm)	21.7	–	15.5	4.7	16.4	4.5	17.0	4.2

the synthesis process could reduce the grain size of ZnO. The grain size of CeO<sub>2</sub> in the as-prepared heterostructures is about 4–5 nm. The weak diffraction peaks of CeO<sub>2</sub> can be attributed to the small grain size of CeO<sub>2</sub> nanoparticles. In fact, doping of Ce into ZnO lattice is not possible due to the difference in the coordination numbers of CeO<sub>2</sub> and ZnO. It is difficult for the eight coordinated Ce presenting in cubic CeO<sub>2</sub> lattice to replace the four coordinated Zn in hexagonal ZnO. Further, in consequence of the high difference in the ionic radius (Zn<sup>2+</sup>, 0.074 nm; Ce<sup>4+</sup>, 0.093 nm), lattice substitution in ZnO by Ce<sup>4+</sup> is highly improbable. The XRD observations indicate that CeO<sub>2</sub>/ZnO heterostructures could be obtained by the facile solid-state reaction method.

To further study the elemental chemical state in the as-prepared CeO<sub>2</sub>/ZnO heterostructures, X-ray photoelectron spectroscopy (XPS) analysis was adopted, and the results are shown in Fig. 3. The survey spectra of 5% CeO<sub>2</sub>/ZnO indicates the existence of Zn, O, Ce and C elements in the 5% CeO<sub>2</sub>/ZnO sample. The C element is ascribed to the adventitious carbon-based additives (binding energy 284.6 eV) and used as reference for calibration. The Zn 2p<sub>3/2</sub> peaks at 1021.08 and 1022.98 eV correspond to Zn–O bonds in the ZnO lattice and Zn<sup>2+</sup> in the zinc-deficient regions. The O 1s spectra could be convoluted into three peaks. The

main signal located at 530.28 eV is the result of O<sup>2-</sup> binding to Zn<sup>2+</sup> in the lattice of ZnO. The peak with a lower binding energy of 528.18 eV is ascribed to the O<sup>2-</sup> in CeO<sub>2</sub> and the leftmost binding energy component at 531.88 eV is attributed to loosely bound oxygen on the surface, such as hydroxyls in oxygen-deficient regions. The surface hydroxyls can produce primary active hydroxyl radicals, which are capable of trapping photoinduced electrons and holes. Thus, the surface hydroxyls are very important for photocatalysis [29]. The Ce 3d spectra of 5% CeO<sub>2</sub>/ZnO is shown in Fig. 3d. The spectrum is composed of two multiplets marked as *p* and *q*, corresponding to the spin-orbit split 3d<sub>3/2</sub> and 3d<sub>5/2</sub> core holes, respectively. A splitting about 18.4 eV between *p*<sub>1</sub> and *q*<sub>1</sub> is observed. The peak at 915.78 eV is the result of Ce<sup>4+</sup> in the as-prepared nanocomposites. The Ce 3d spectra is in good agreement with other authors [30–32], which proved cerium element exists as CeO<sub>2</sub> in 5% Ce/ZnO sample. Hence, we have successfully synthesized CeO<sub>2</sub>/ZnO heterostructures by the facile solid-state reaction method.

Figure 4 shows SEM images of CeO<sub>2</sub>/ZnO heterostructures with different molar contents of CeO<sub>2</sub>. It indicates that the heterostructures consist of clustered nanorods or nanosheets and the amount of CeO<sub>2</sub> plays an important role in controlling the morphology of products. As

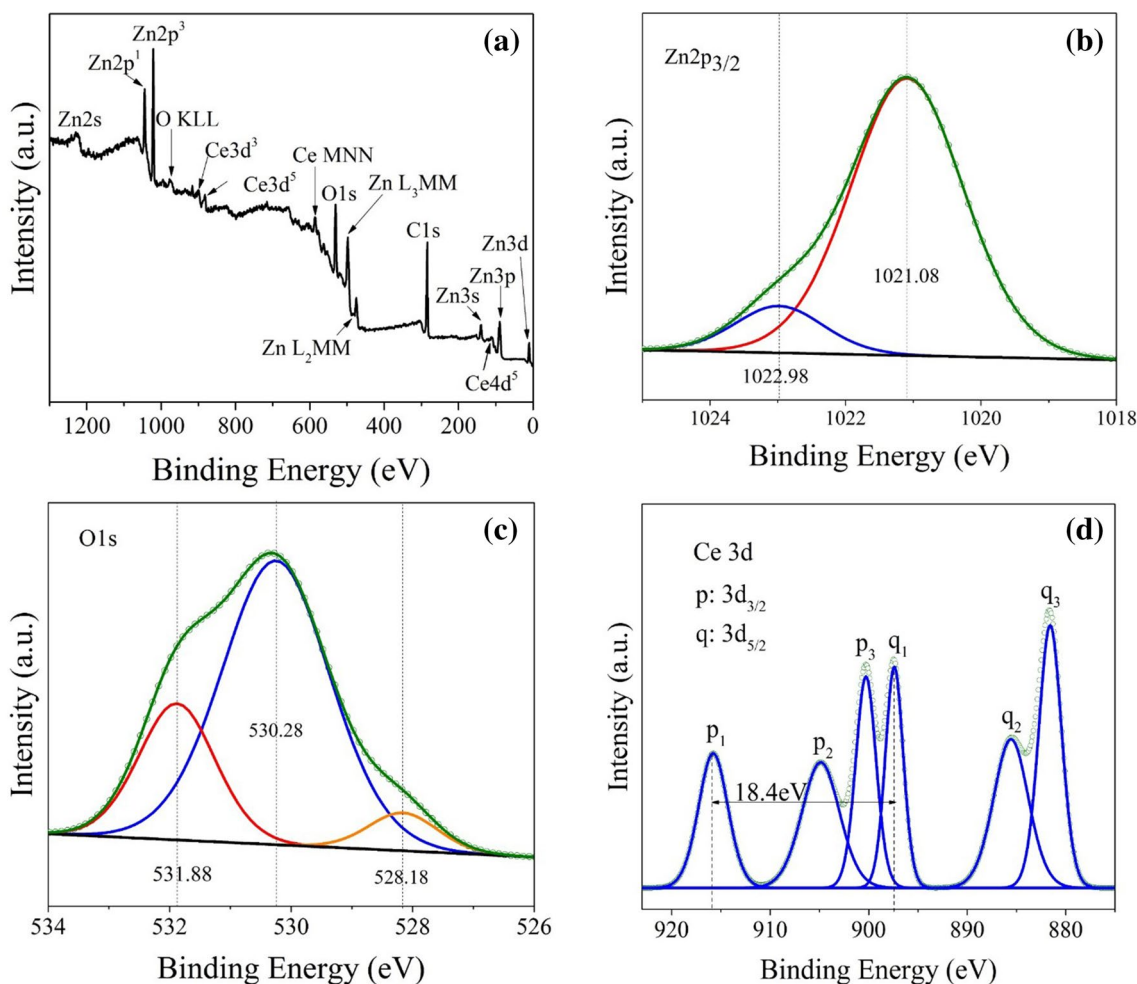


**Fig. 3** XPS spectra of 5% CeO<sub>2</sub>/ZnO: **a** fully scanned spectra, **b** Zn2p<sub>3/2</sub>, **c** O1s, **d** Ce3d

observed in Fig. 4a, pure ZnO is formed by irregular bulks aggregated with small particles and short nanorods. Then nanorods on the surface of catalysts become longer with increasing amount of CeO<sub>2</sub> as shown in Fig. 4b, c. The lengths of the nanorods in 2% CeO<sub>2</sub>/ZnO and 5% CeO<sub>2</sub>/ZnO are 150–200 nm and 300–500 nm, respectively. It indicates CeO<sub>2</sub> would promote the growth of the nanorods. When the molar ratio of CeO<sub>2</sub> reaches 10%, the morphology turns into nanosheets sticking together, as Fig. 4d displayed. The length and width of the nanosheets in 10% CeO<sub>2</sub>/ZnO is about 200–300 nm. The thickness of the sheet is about 30–40 nm. The SEM observation demonstrates that the amount of CeO<sub>2</sub> has a great impact on the micromorphology of the CeO<sub>2</sub>/ZnO heterostructures. Impurities introduced in the synthesis process could greatly influence the morphology of ZnO [33]. The addition of CeO<sub>2</sub> will influence the nucleation and growth of ZnO in the synthesis process. Full width at half maximum (FWHM) of (100), (002) and (101) peak of ZnO is used to characterize the crystalline features of ZnO, as shown

in Fig. 1b. In ZnO, the FWHM of (100), (002) and (101) peak is all very low, especially for (002) peak. This results in the uniform growth of ZnO in all directions or a little degree of oriented growth in the (002) lattice plane. Thus, pure ZnO is formed by irregular bulks aggregated with small particles and short nanorods. After addition of a small quantity of CeO<sub>2</sub> in 2% CeO<sub>2</sub>/ZnO sample, the FWHM of (100) and (101) peak sharply increased from 0.43 to 0.77 and from 0.43 to 0.74, respectively. However, the FWHM of (002) peak is still very low. It suggests that CeO<sub>2</sub> would suppress the growth of ZnO in [100] and [101] crystallographic direction without disturbing the growth in [002] direction, which results 2% CeO<sub>2</sub>/ZnO sample in a nanorod-like morphology. With further increasing the amount of CeO<sub>2</sub> in 5% CeO<sub>2</sub>/ZnO and 10% CeO<sub>2</sub>/ZnO sample, the FWHM of (002) peak still remains stable. Nevertheless, the FWHMs of (100) and (101) peak both slightly decreased. It implies that the suppression to the growth of [100] and [101] crystallographic direction is weakened by further increasing the amount of CeO<sub>2</sub>.

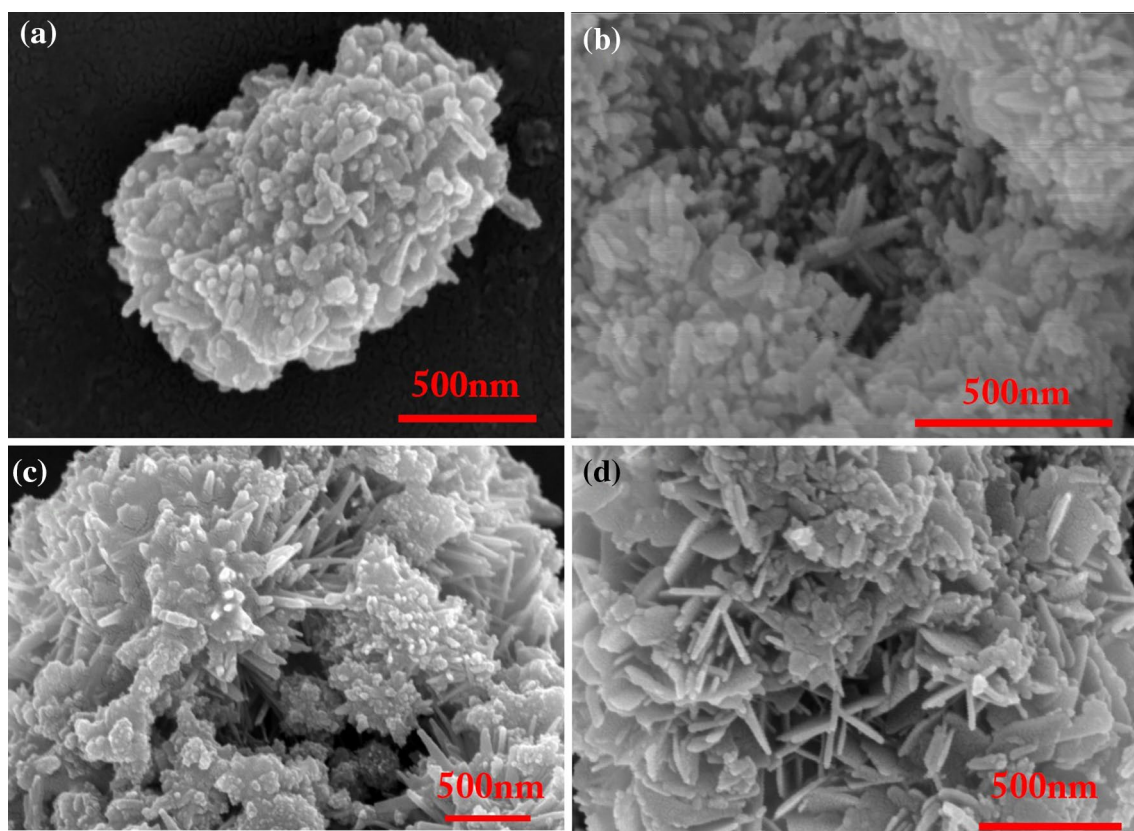


**Fig. 4** SEM images of **a** pure ZnO, **b** 2% CeO<sub>2</sub>/ZnO, **c** 5% CeO<sub>2</sub>/ZnO and **d** 10% CeO<sub>2</sub>/ZnO

Thus, 5% CeO<sub>2</sub>/ZnO displays a narrow nanosheet-like or nanorod-like morphology and large sheets are formed in 10% CeO<sub>2</sub>/ZnO sample.

Morphology changes of CeO<sub>2</sub>/ZnO lead to increased specific surface area. The specific surface area of ZnO and 5% CeO<sub>2</sub>/ZnO is 16.55 and 20.11 m<sup>2</sup>/g, respectively. It indicates that addition of CeO<sub>2</sub> in ZnO could increase the specific surface area of the catalyst, thus provides more active spots for the photocatalytic reaction. The existence of Zn, O, Ce elements in 5% CeO<sub>2</sub>/ZnO is also evidenced in the element mappings, as Fig. 5 displays. It indicates that CeO<sub>2</sub> is uniformly dispersed in 5% CeO<sub>2</sub>/ZnO sample, instead of forming aggregates of irregular bulks.

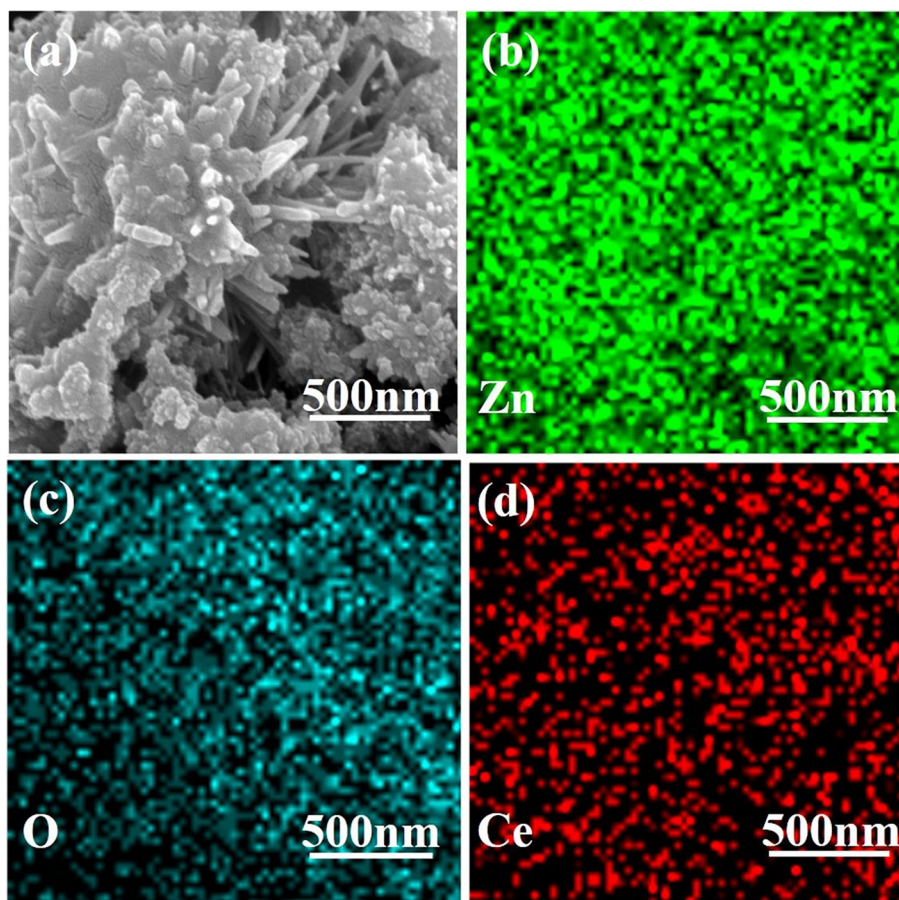
The morphologies of pure ZnO and 5% CeO<sub>2</sub>/ZnO are further investigated by TEM and HRTEM. As can be seen from Fig. 6a, c, pure ZnO and 5% CeO<sub>2</sub>/ZnO are both consisting clustered nanorods, while the nanorods in 5% CeO<sub>2</sub>/ZnO are much longer than that in pure ZnO. The high-magnification image in Fig. 6d clearly demonstrates the formation of CeO<sub>2</sub>/ZnO heterojunction. The interplanar spacings between adjacent lattice fringes are 0.26 and 0.32 nm, which represent the (001) crystal plane of hexagonal wurtzite ZnO and (111) of fluorite CeO<sub>2</sub>, respectively. The grain size of CeO<sub>2</sub> in 5% CeO<sub>2</sub>/ZnO are about 5 nm in length and 3 nm

in width, which is in good accordance with the calculated results from the XRD analysis.

To evaluate the photo-absorption behaviors of the CeO<sub>2</sub>/ZnO heterostructures, the room-temperature UV–visible diffuse reflectance spectra was carried out and the results are shown in Fig. 7a. Pure ZnO only responded to ultraviolet light (band edge absorption around 390 nm), while 5% CeO<sub>2</sub>/ZnO sample showed absorption peaks both in the UV and visible region. CeO<sub>2</sub> displayed a further extended visible light absorbance. The inset of Fig. 7a is the corresponding Kubelka–Munk plots of ZnO and CeO<sub>2</sub>. The calculated band gaps of ZnO and CeO<sub>2</sub> are 3.20 and 2.76 eV, respectively. Thus, the formation of heterostructures with CeO<sub>2</sub> is an effective way to enhance the photo-absorption property of ZnO.

Photoluminescence emission spectra was obtained to investigate the role of CeO<sub>2</sub> in the heterojunction in the processes of charge migration, transfer and separation. As shown in Fig. 7b, the UV emission, centered at around 390 nm (3.2 eV), is the exact recombination related near-band edge emission or free exciton emission of ZnO. Several satellite peaks in the visible range are observed which are ascribed to the defects, like oxygen vacancies, in the catalysts [34–36]. Oxygen vacancies could serve as

**Fig. 5** SEM and corresponding EDS mapping images of 5% CeO<sub>2</sub>/ZnO heterostructures



photoinduced charge traps, and also adsorption sites where the charge transfers to adsorbed species, which can reduce photoinduced electron–hole pair recombination. Compared with pure ZnO, the quenched peaks of 5% CeO<sub>2</sub>/ZnO indicates the suppressed recombination of photo-induced electrons and holes. It demonstrates that the formation of heterostructures greatly enhanced the charge separation efficiency of the photo-induced electrons and holes.

The electrochemical impedance spectroscopy (EIS) is used to investigate the electrical conductivity of the samples. As shown in Fig. 8a, the decreased arc radius of Nyquist plot for CeO<sub>2</sub>/ZnO heterostructures suggests a smaller charge transfer resistance compared with pure ZnO. This is also evidenced by the transient photocurrent response test (Fig. 8b). The photocurrent of 5% CeO<sub>2</sub>/ZnO is twice more than that of pure ZnO. In addition, 5% CeO<sub>2</sub>/ZnO also has faster photo-response rate. It indicates that CeO<sub>2</sub>/ZnO heterojunction has greater electronic transportation ability than that of pure ZnO. Hence, the CeO<sub>2</sub>/ZnO heterostructures are beneficial for photocatalysis.

The decomposition of RhB was carried out to evaluate the photocatalytic properties of the as-prepared CeO<sub>2</sub>/ZnO heterostructures. Figure 9a presents the degradation profiles of RhB over four samples. The blank experiments are

also performed to demonstrate that the photoinduced self-degradation could be ignored with respect to that caused by photo degradation. As observed in the plot, the photocatalytic properties of the heterojunctions first increase and then decrease when an increasing amount of CeO<sub>2</sub> is introduced in the system. 5% CeO<sub>2</sub>/ZnO, which can decompose RhB completely (95%) in 90 min, shows the highest photocatalytic activity. For better understanding the difference between the four samples, corresponding kinetic linear simulation curves are shown in Fig. 9b. The apparent rate constants were calculated by Langmuir–Hinshelwood equation which could be described as:

$$\ln(C/C_0) = -k_{\text{app}}t \quad (1)$$

where  $k_{\text{app}}$  is the degradation rate constant,  $C_0$  and  $C$  are the initial concentration of RhB and that after reaction time  $t$ . The calculated value of apparent rate constants are 0.00731, 0.01025, 0.03319 and 0.00675 min<sup>-1</sup> for ZnO, 2, 5 and 10% CeO<sub>2</sub>/ZnO, respectively. Table 2 shows the apparent first-order rate constants of 5% CeO<sub>2</sub>/ZnO and other reported CeO<sub>2</sub>/ZnO heterostructures. The temporal evolution of the spectral changes upon the photodegradation of RhB is shown in Fig. 9c. The absorption peak can hardly be found after

**Fig. 6** TEM and HRTEM images of **a, b** ZnO and **c, d** 5% CeO<sub>2</sub>/ZnO

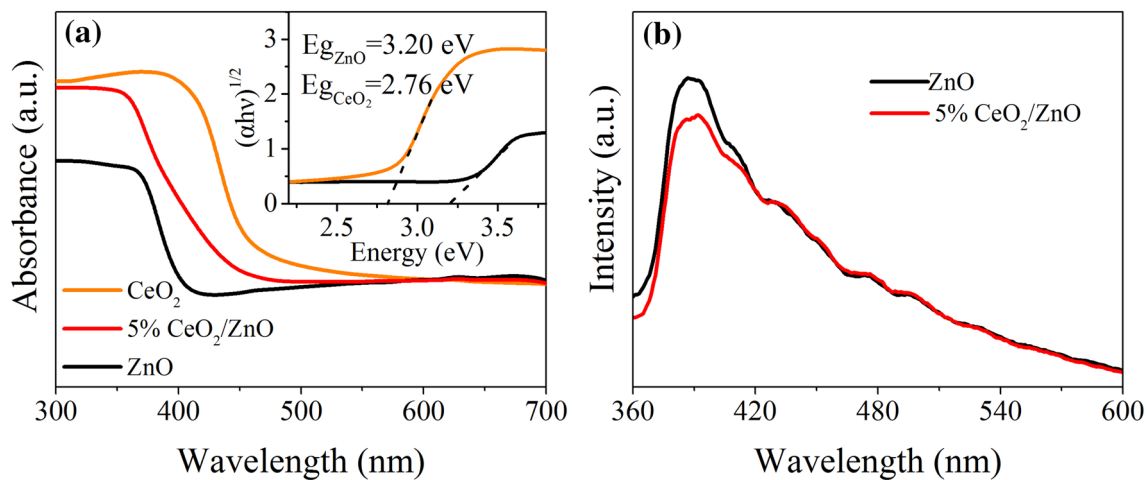
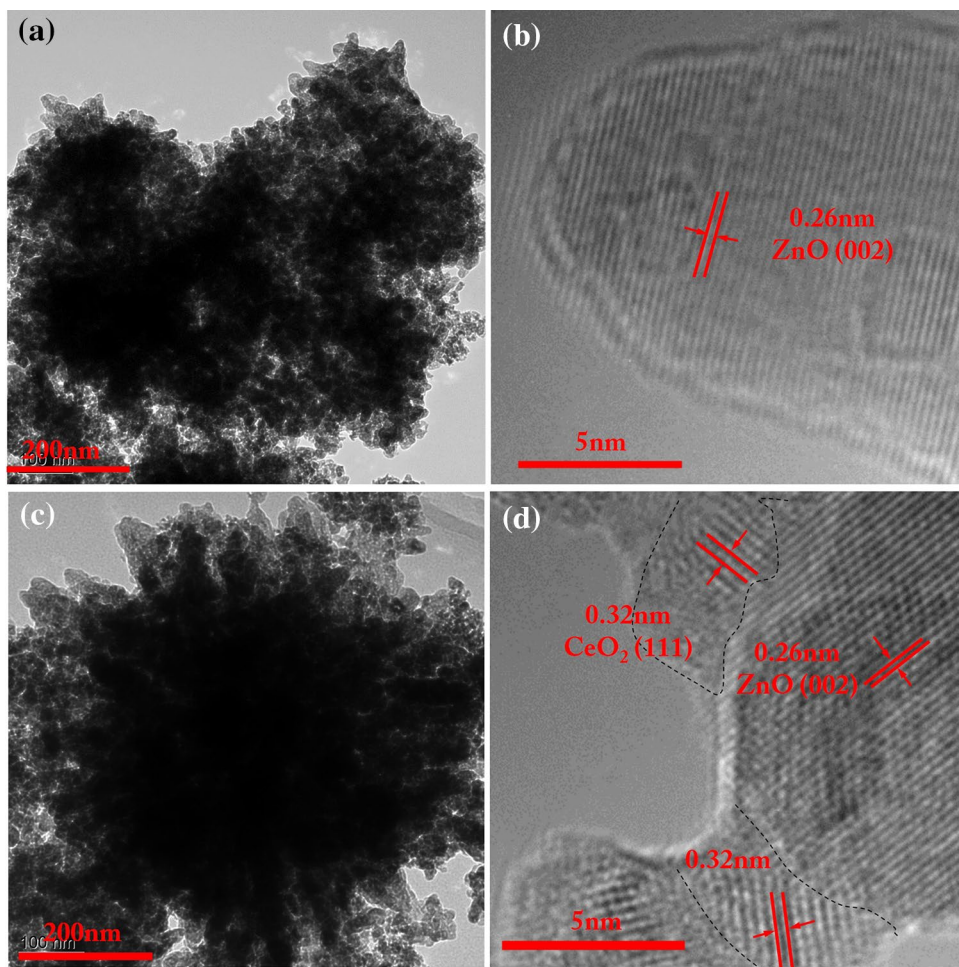


**Fig. 7** **a** UV-visible absorption spectra of ZnO, 5% CeO<sub>2</sub>/ZnO and CeO<sub>2</sub>, the insert shows the corresponding Kubelka–Munk plots of ZnO and CeO<sub>2</sub>; **b** fluorescence emission spectra of ZnO and 5% CeO<sub>2</sub>/ZnO

120 min in the presence of 5% CeO<sub>2</sub>/ZnO catalyst. While pure ZnO could only decompose 56% of the RhB solution. No shift of peaks or new peaks were observed indicating the

RhB was not transformed into other organic compounds but directly decomposed into inorganic substance, for instance, CO<sub>2</sub> and H<sub>2</sub>O. The reason for performance loss of 10%

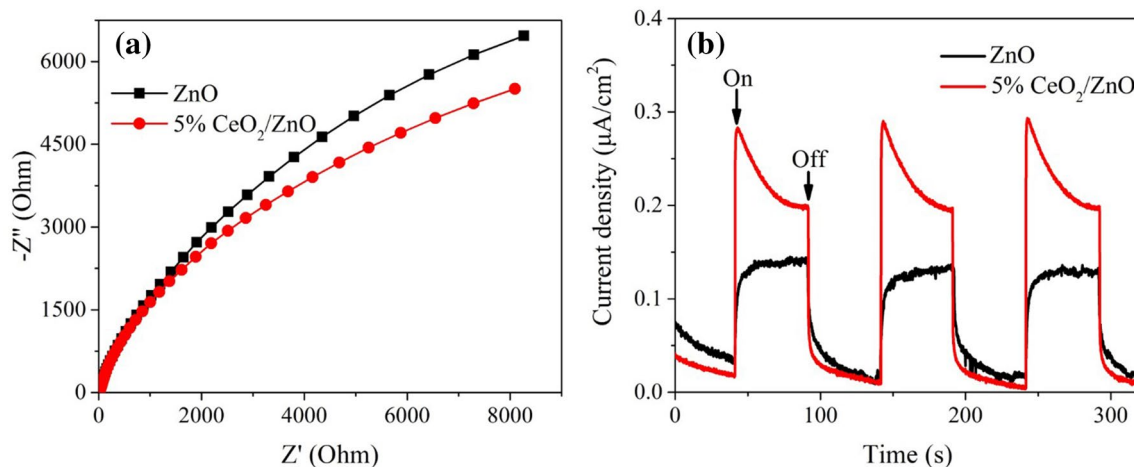


Fig. 8 a Nyquist impedance plots and b transient photocurrents as a function of incident light for ZnO and 5% CeO<sub>2</sub>/ZnO

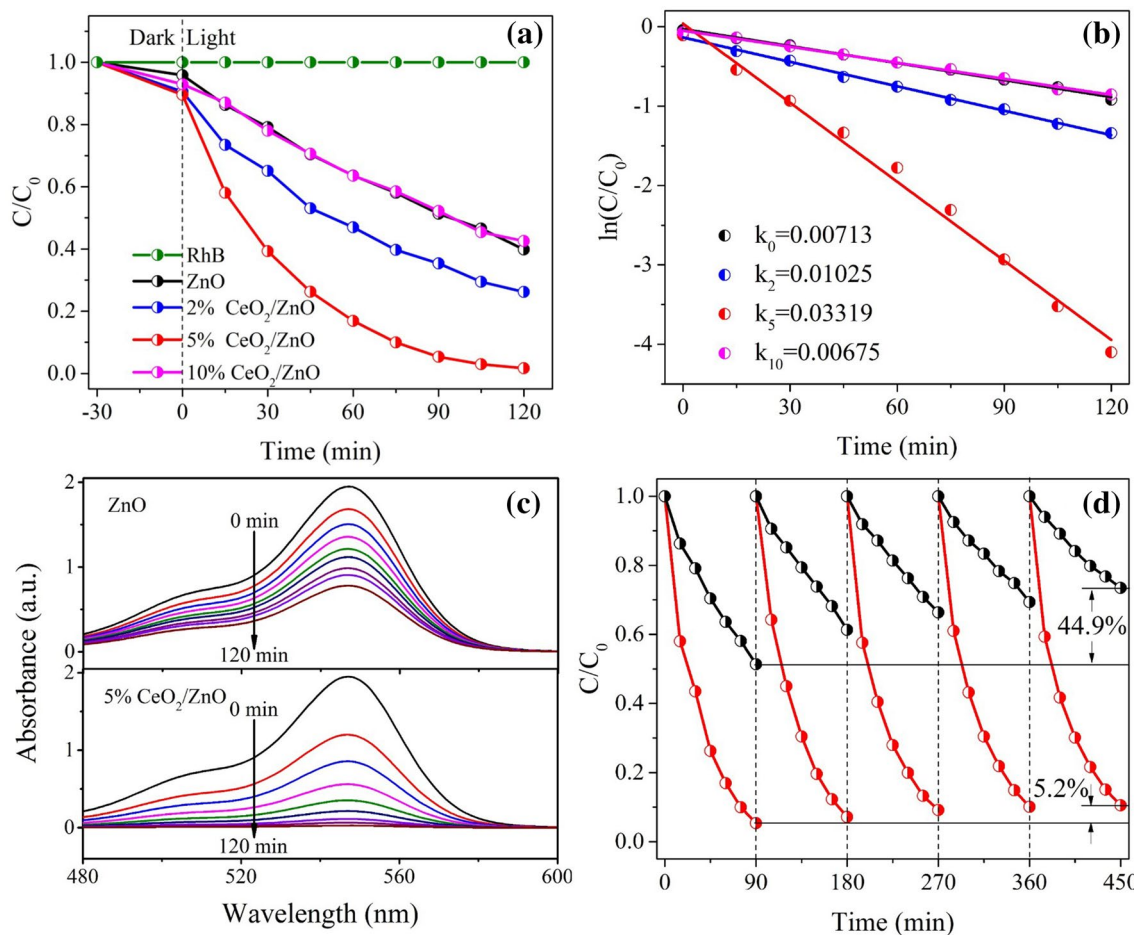


Fig. 9 a Photodegradation profiles of RhB over CeO<sub>2</sub>/ZnO heterostructures with different amount of CeO<sub>2</sub>, b kinetic linear simulation curves of RhB photocatalytic degradation with four samples, c UV-

Vis spectra of RhB solution reduction by ZnO and 5% CeO<sub>2</sub>/ZnO, and d cycling runs in the photocatalytic degradation of RhB by ZnO and 5% CeO<sub>2</sub>/ZnO



**Table 2** Apparent rate constants ( $k_{app}$ ) for 5% CeO<sub>2</sub>/ZnO and comparison with other reported CeO<sub>2</sub>/ZnO heterostructures

Chemical	Preparation	$k_{app}$ (min <sup>-1</sup> )	Morphology	Ref.
CeO <sub>2</sub> /ZnO	Solid state reaction (RT)	0.03319	Nanorod cluster	This work
CeO <sub>2</sub> /ZnO	Electrospinning + calcination (600 °C)	0.02107	Nanofiber	[27]
CeO <sub>2</sub> /ZnO	Solution method + calcination (400 °C)	0.01612	Nanoparticle	[28]
CeO <sub>2</sub> /ZnO	Wet-chemical method (90 °C)	0.00772	Microprism	[36]

CeO<sub>2</sub>/ZnO could be that excess amount of CeO<sub>2</sub> on the surface of the photocatalyst covered a large amount of active spots on ZnO. Consequently, a decrease amount of ZnO is excited and less photogenerated carriers would be obtained when an overdose of CeO<sub>2</sub> is introduced.

To demonstrate the stability and potential applicability of the as-synthesised CeO<sub>2</sub>/ZnO heterostructures, cycle experiment was performed on ZnO and 5% CeO<sub>2</sub>/ZnO sample. A significant photocorrosion effect was observed in ZnO. After five cycling reuse, a decrease about 44.9% (from 49 to 26%) was obtained on the photocatalytic efficiency of ZnO. While the photocatalytic efficiency of 5% CeO<sub>2</sub>/ZnO catalyst for five cycling reuse was 95, 93, 91, 90 and 89% after 90 min, respectively. Only 5.2% of decrease is observed after five runs. It is well known that ZnO displays a severe photocorrosion effect when exposed to holes in aqueous solution [37]. Chen et al. and Han et al. reported that formation of heterostructures with carbonaceous materials can greatly enhance the anti-photocorrosion performance of ZnO [38, 39]. In our case, the cycling run results indicate that coupling with CeO<sub>2</sub>, a rare earth oxide, can also greatly improve the stability and photocorrosion resistance performance of ZnO.

The radicals and holes trapping experiments were designed on 5% CeO<sub>2</sub>/ZnO sample to study the photodegradation process of CeO<sub>2</sub>/ZnO heterostructure. As shown in Fig. 10a, the photocatalytic process of CeO<sub>2</sub>/ZnO heterojunction is totally inhibited by the addition of ethylenediaminetetraacetic acid disodium salt (EDTA-2Na), a strong hole scavenger. It indicates that the photogenerated hole is the main active species that can oxidize the adsorbed RhB dye into inorganic substance. The photocatalytic degradation rate changes distinctively when a hydroxyl radical ( $\bullet$ OH) scavenger, tert-butanol (t-BuOH), is injected in the system. After 90 min of irradiation, the RhB degraded only 47%. The results demonstrate that the surface hydroxyls of photocatalyst are also very crucial. To observe the photogenerated radical species, UV-Vis spectrophotometry was carried out. Nitrotetrazolium blue chloride (NBT) can react with superoxide radical (O<sub>2</sub><sup>-</sup>) to produce tetrazolium blue diformazan (BTDF), which shows an absorption peak at 560 nm [40]. The quantity of O<sub>2</sub><sup>-</sup> can be assessed by the intensity of absorption peak. On the other hand, salicylic acid (SA), which displays an absorption peak at 303 nm, can react with hydroxyl radical ( $\bullet$ OH) and produce 2,3-dihydroxybenzoic acid (2,3-DHBA) [41]. Due

to the absorption peak of 2,3-DHBA at 310 nm is rather low and could be disturbed by the absorbance of SA, we used the absorption of SA at 303 nm to observe the generation of  $\bullet$ OH. The reactions of NBT with superoxide radical and SA with hydroxyl radical are shown in Fig. 10c. As shown in Fig. 10b, the absorbance at 303 nm decreased and that at 560 nm increased linearly with time when the solution is exposed to light. It indicates that NBT reacted with O<sub>2</sub><sup>-</sup> and produced BTDF, while SA was turned into 2,3-DHBA by  $\bullet$ OH. The concentration of BTDF and SA did not change in dark according to the horizontal absorbance plot. This demonstrates that the O<sub>2</sub><sup>-</sup> and  $\bullet$ OH were photo-induced, but not generated by other pathway.

Figure 11 is the schematic diagram of photocatalytic mechanism for CeO<sub>2</sub>/ZnO heterostructures. Band energy positions of CeO<sub>2</sub> and ZnO are required to establish the coupled semiconductor mechanism. To obtain the exact band positions of CeO<sub>2</sub>, we followed the method used by Xu and Schoonen [42]. It has been confirmed for more than 30 oxide and sulfide semiconductors and was found to be in well agreement with the experimental results. According to this method, the electronegativity ( $\chi$ ), electron affinity (EA) and ionization energy (IE) values of the semiconductor are equivalent to that of the Fermi level energy, CB energy and VB energy, respectively. The VB energy and CB energy could be calculated using

$$IE(\text{ZnO}) = E_{\text{VB}}(\text{ZnO}) = \chi(\text{ZnO}) + 1/2E_g, \quad (2)$$

$$EA(\text{ZnO}) = E_{\text{CB}}(\text{ZnO}) = \chi(\text{ZnO}) - 1/2E_g. \quad (3)$$

The values of valance band energy and conduction band energy obtained are in absolute vacuum scale (AVS), and can be converted to the normal hydrogen electrode (NHE) using

$$E_{\text{CB}}(\text{ZnO})_{(\text{NHE})} = E_{\text{CB}}(\text{ZnO})_{(\text{AVS})} - 4.5 \text{ eV}. \quad (4)$$

The values of VB and CB band positions calculated according to the above equations are listed in Table 3. The results show that both VB and CB energy of CeO<sub>2</sub> are more negative than that of ZnO. After the contract of CeO<sub>2</sub> and ZnO, the photoinduced electrons will transfer from CB of CeO<sub>2</sub> to that of ZnO, and holes will transfer from VB of ZnO

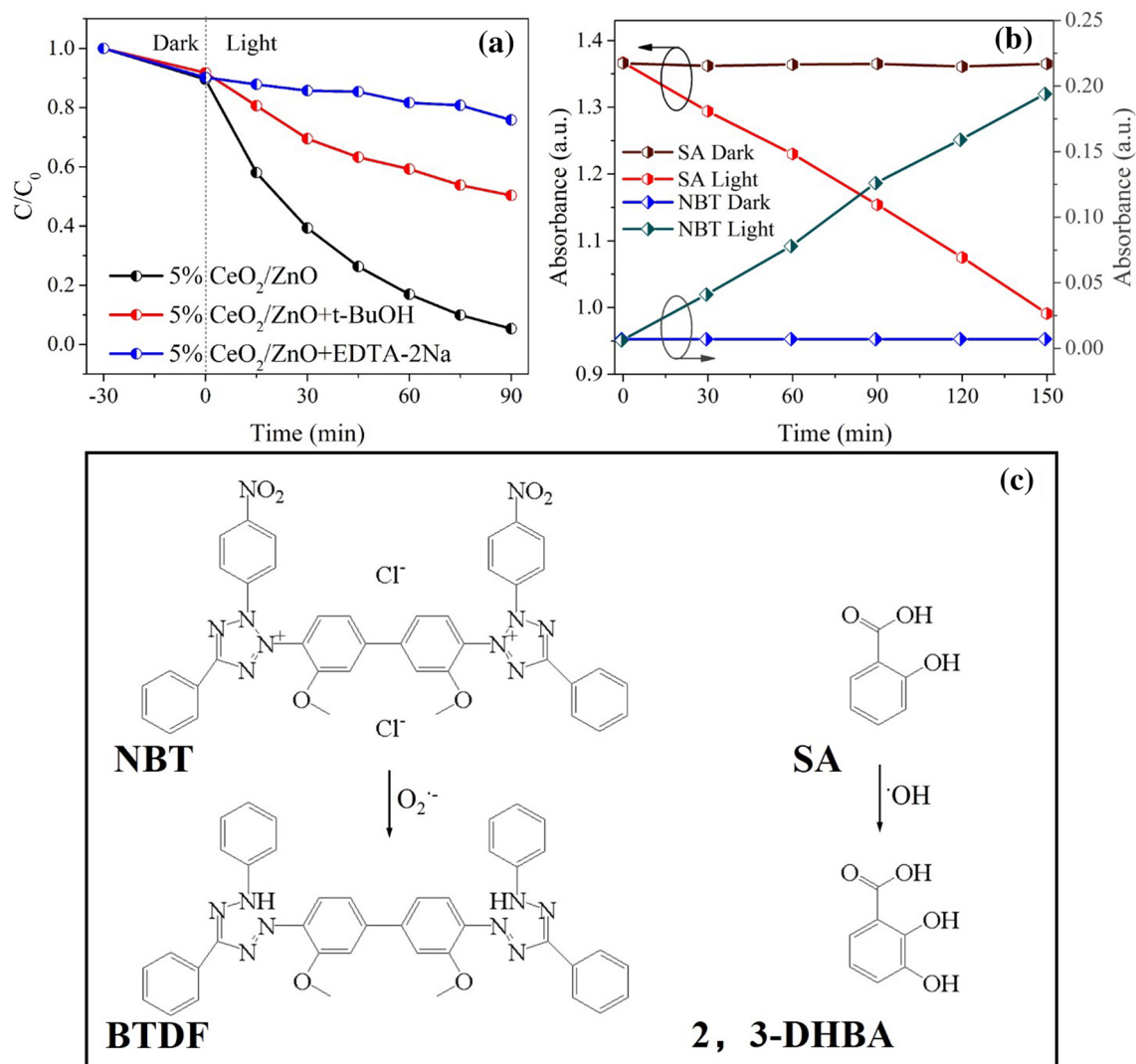


**Fig. 10** **a** Plots of photogenerated carrier trapping experiment in the degradation of RhB with EDTA-2Na (0.1 M) and t-BuOH (0.1 M), **b** time dependencies of absorbance at 303 nm for SA and 560 nm for

BTDF, and **c** reactions of NBT with superoxide radical and SA with hydroxyl radical

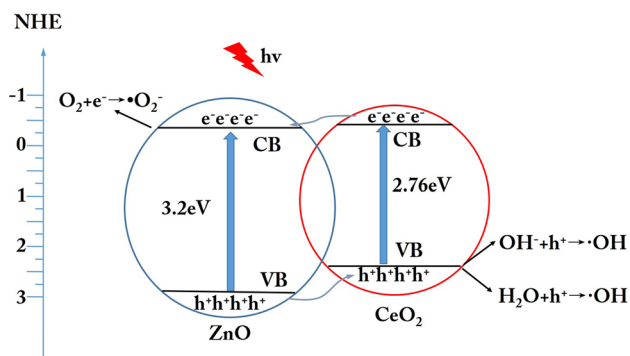


**Fig. 11** Scheme for the photocatalytic reaction of the CeO<sub>2</sub>/ZnO heterostructures

**Table 3** Calculated band gap, valence and conduction band energy of CeO<sub>2</sub> and ZnO

Semiconductor	Band gap (eV)	$E_{VB}$ (V)	$E_{CB}$ (V)
ZnO	3.20	-0.31	2.89
CeO <sub>2</sub>	2.76	-0.32	2.44

to CeO<sub>2</sub> spontaneously. Thus, the formation of CeO<sub>2</sub>/ZnO heterojunction would facilitate the transport of photogenerated carriers. The photoinduced electrons and holes could also be separated efficiently. Then, the holes at the VB of CeO<sub>2</sub>, as main oxidative species, could directly oxidize the RhB or generate hydroxyls, which are also strong oxidants and could oxidize the dye into inorganic compounds.

## 4 Conclusions

CeO<sub>2</sub>/ZnO heterostructures were successfully fabricated by a solid-state reaction method at room temperature without any surfactant or template. The amount of CeO<sub>2</sub> plays an important role in controlling the morphology of the as-prepared nanostructures. The introduction of CeO<sub>2</sub> would enhance the photo-absorption property, accelerate the migration of photogenerated carriers, increase the specific surface area from 16.55 to 20.11 m<sup>2</sup>/g and suppress the recombination of electrons and holes, thus enhance the photocatalytic activity of ZnO. The 5% CeO<sub>2</sub>/ZnO shows the highest photocatalytic activity and has a degradation rate constant of 0.03319 which is four times more than that of ZnO. The CeO<sub>2</sub>/ZnO heterojunctions also possess high stability and photocorrosion resistance. It demonstrates that the CeO<sub>2</sub>/ZnO heterostructure prepared under present approach is a promising candidate for scale-up industrial application in photocatalysis.

**Acknowledgements** This work is supported by the National Nature Science Foundation (51672220), the 111 Program (B08040) of MOE, the National Defense Science Foundation (32102060303), the Xi'an Science and Technology Foundation (CX Y1706-5, 2017086CGRC049-XBGY005), the Shaanxi Provincial Science Foundation (2017KW-018), and the NPU Gaofeng Project (17GH020824) of China.

## References

1. B. Cheng, Y. Le, J. Yu, Preparation and enhanced photocatalytic activity of Ag@TiO<sub>2</sub> core-shell nanocomposite nanowires. *J. Hazard. Mater.* **177**, 971–977 (2010)
2. L. Huang, H. Fan, Room-temperature solid state synthesis of ZnO/α-Fe<sub>2</sub>O<sub>3</sub> hierarchical nanostructures and their enhanced gas-sensing properties. *Sensor. Actuat. B Chem.* **171–172**, 1257–1263 (2012)
3. J. Fang, H. Fan, G. Dong, A facile way to synthesize cost-effective ZnO nanorods with enhanced photocatalytic activity. *Mater. Lett.* **120**, 147–150 (2014)
4. Z.P. Sun, L. Liu, L. Zhang, D.Z. Jia, Rapid synthesis of ZnO nanorods by one-step, room-temperature, solid-state reaction and their gas-sensing properties. *Nanotechnology* **17**, 2266–2270 (2006)
5. M. Law, L.E. Greene, J.C. Johnson, R. Saykally, P. Yang, Nanowire dye-sensitized solar cells. *Nat. Mater.* **4**, 455–459 (2005)
6. C. Tian, Q. Zhang, A. Wu, M. Jiang, Z. Liang, B. Jiang, H. Fu, Cost-effective large-scale synthesis of ZnO photocatalyst with excellent performance for dye photodegradation. *Chem. Commun.* **48**, 2858–2860 (2012)
7. J. Yu, X. Yu, Hydrothermal synthesis and photocatalytic activity of zinc oxide hollow spheres. *Environ. Sci. Technol.* **42**, 4902–4907 (2008)
8. M.M. Ba-Abbad, A.A. Kadhum, A.B. Mohamad, M.S. Takriff, K. Sopian, Visible light photocatalytic activity of Fe<sup>3+</sup>-doped ZnO nanoparticle prepared via sol-gel technique. *Chemosphere* **91**, 1604–1611 (2013)
9. X. Li, Z. Hu, J. Liu, D. Li, X. Zhang, J. Chen, J. Fang, Ga doped ZnO photonic crystals with enhanced photocatalytic activity and its reaction mechanism. *Appl. Catal. B Environ.* **195**, 29–38 (2016)
10. W. Tabib, B. Bouzlama, A. Sieber, H. Addad, M. Elhouichet, R. Férid, Boukherroub, Structural and optical properties of Na doped ZnO nanocrystals: application to solar photocatalysis. *Appl. Surf. Sci.* **396**, 1528–1538 (2017)
11. Wu, Facile one-step synthesis of N-doped ZnO micropolyhedrons for efficient photocatalytic degradation of formaldehyde under visible-light irradiation. *Appl. Surf. Sci.* **319**, 237–243 (2014)
12. J. Fang, H. Fan, Y. Ma, Z. Wang, Q. Chang, Surface defects control for ZnO nanorods synthesized by quenching and their anti-recombination in photocatalysis. *Appl. Surf. Sci.* **332**, 47–54 (2015)
13. J. Wang, Y. Xia, Y. Dong, R. Chen, L. Xiang, S. Komarneni, Defect-rich ZnO nanosheets of high surface area as an efficient visible-light photocatalyst. *Appl. Catal. B Environ.* **192**, 8–16 (2016)
14. X. Bai, L. Wang, R. Zong, Y. Lv, Y. Sun, Y. Zhu, Performance enhancement of ZnO photocatalyst via synergic effect of surface oxygen defect and graphene hybridization. *Langmuir* **29**, 3097–3105 (2013)
15. H. Zeng, P. Liu, W. Cai, S. Yang, X. Xu, Controllable Pt/ZnO porous nanocages with improved photocatalytic activity. *J. Phys. Chem. C* **112**, 19620–19624 (2008)
16. W. He, H.K. Kim, W.G. Wamer, D. Melka, J.H. Callahan, J.J. Yin, Photogenerated charge carriers and reactive oxygen species in ZnO/Au hybrid nanostructures with enhanced photocatalytic and antibacterial activity. *J. Am. Chem. Soc.* **136**, 750–757 (2014)
17. O.K. Ranasingha, C. Wang, P.R. Ohodnicki, J.W. Lekse, J.P. Lewis, C. Matranga, Synthesis, characterization, and photocatalytic activity of Au–ZnO nanopyrramids. *J. Mater. Chem. A* **3**, 15141–15147 (2015)
18. R. Zou, G. He, K. Xu, Q. Liu, Z. Zhang, J. Hu, ZnO nanorods on reduced graphene sheets with excellent field emission, gas sensor and photocatalytic properties. *J. Mater. Chem. A* **1**, 8445 (2013)
19. X. Wang, P. Ren, H. Fan, Room-temperature solid state synthesis of ZnO/Bi<sub>2</sub>O<sub>3</sub> heterojunction and their solar light photocatalytic performance. *Mater. Res. Bull.* **64**, 82–87 (2015)
20. Y. Li, B.P. Zhang, J.X. Zhao, Z.H. Ge, X.K. Zhao, L. Zou, ZnO/carbon quantum dots heterostructure with enhanced photocatalytic properties. *Appl. Surf. Sci.* **279**, 367–373 (2013)
21. R. Sasikala, A.P. Gaikwad, V. Sudarsan, N. Gupta, S.R. Bharadwaj, Cubic phase indium doped cadmium sulfide dispersed on zinc oxide: enhanced photocatalytic activity for hydrogen generation from water. *Appl. Catal. A Gen.* **464–465**, 149–155 (2013)
22. M.Q. Yang, N. Zhang, Y. Wang, Y.J. Xu, Metal-free, robust, and regenerable 3D graphene-organics aerogel with high and stable photosensitization efficiency. *J. Catal.* **346**, 21–29 (2017)
23. M.Q. Yang, C. Han, N. Zhang, Y.J. Xu, Precursor chemistry matters in boosting photoredox activity of graphene/semiconductor composites. *Nanoscale* **7**, 18062–18070 (2015)
24. C. Han, Z. Chen, N. Zhang, J.C. Colmenares, Y.J. Xu, Hierarchically CdS decorated 1D ZnO nanorods-2D graphene hybrids: low temperature synthesis and enhanced photocatalytic performance. *Adv. Funct. Mater.* **25**, 221–229 (2015)
25. N. Zhang, S. Liu, X. Fu, Y.J. Xu, A simple strategy for fabrication of “plum-pudding” type Pd@CeO<sub>2</sub> semiconductor nanocomposite as a visible-light-driven photocatalyst for selective oxidation. *J. Phys. Chem. C* **115**, 22901–22909 (2011)
26. D. Channei, B. Inceesungvorn, N. Wetchakun, S. Ukritnukun, A. Nattestad, J. Chen, S. Phanichphant, Photocatalytic degradation of methyl orange by CeO<sub>2</sub> and Fe-doped CeO<sub>2</sub> films under visible light irradiation. *Sci. Rep.* **4**, 5757 (2014)
27. C. Li, R. Chen, X. Zhang, S. Shu, J. Xiong, Y. Zheng, W. Dong, Electrospinning of CeO<sub>2</sub>-ZnO composite nanofibers and their photocatalytic property. *Mater. Lett.* **65**, 1327–1330 (2011)

28. M. Faisal, S.B. Khan, M.M. Rahman, A. Jamal, A.M. Asiri, M.M. Abdullah, Smart chemical sensor and active photocatalyst for environmental pollutants. *Chem. Eng. J* **173**, 178–184 (2011)
29. W. Lu, S. Gao, J. Wang, One-pot synthesis of Ag/ZnO self-assembled 3D hollow microspheres with enhanced photocatalytic performance. *J. Phys. Chem. C* **112**, 16792–16800 (2008)
30. E. Bêche, P. Charvin, D. Perarnau, S. Abanades, G. Flamant, Ce 3d XPS investigation of cerium oxides and mixed cerium oxide ( $Ce_xTi_yO_z$ ). *Surf. Interface Anal.* **40**, 264–267 (2008)
31. L. Qiu, F. Liu, L. Zhao, Y. Ma, J. Yao, Comparative XPS study of surface reduction for nanocrystalline and microcrystalline ceria powder. *Appl. Surf. Sci* **252**, 4931–4935 (2006)
32. Q.X. Zhao, P. Klason, M. Willander, H.M. Zhong, W. Lu, J.H. Yang, Deep-level emissions influenced by O and Zn implantations in ZnO. *Appl. Phys. Lett.* **87**, 211912 (2005)
33. X. Jia, H. Fan, M. Afzaal, X. Wu, P. O'Brien, Solid state synthesis of tin-doped ZnO at room temperature: characterization and its enhanced gas sensing and photocatalytic properties. *J. Hazard. Mater.* **193**, 194–199 (2011)
34. H. Faber, J. Hirschmann, M. Klaumunzer, B. Braunschweig, W. Peukert, M. Halik, Impact of oxygen plasma treatment on the device performance of zinc oxide nanoparticle-based thin-film transistors. *ACS Appl. Mater. Inter.* **4**, 1693–1696 (2012)
35. X.P. Shen, A.H. Yuan, Y.M. Hu, Y. Jiang, Z. Xu, Z. Hu, Fabrication, characterization and field emission properties of large-scale uniform ZnO nanotube arrays. *Nanotechnology* **16**, 2039–2043 (2005)
36. I.T. Liu, M.H. Hon, L.G. Teoh, The preparation, characterization and photocatalytic activity of radical-shaped  $CeO_2/ZnO$  microstructures. *Ceram. Int.* **40**, 4019–4024 (2014)
37. K. Dai, G. Dawson, S. Yang, Z. Chen, L.H. Lu, Large scale preparing carbon nanotube/zinc oxide hybrid and its application for highly reusable photocatalyst. *Chem. Eng. J.* **191**, 571–578 (2012)
38. Z. Chen, N. Zhang, Y.J. Xu, Synthesis of graphene-ZnO nanorod nanocomposites with improved photoactivity and anti-photocorrosion. *Cryst. Eng. Comm.* **15**, 3022–3030 (2013)
39. C. Han, M.Q. Yang, B. Weng, Y.J. Xu, Improving the photocatalytic activity and anti-photocorrosion of semiconductor ZnO by coupling with versatile carbon. *Phys. Chem. Chem. Phys.* **16**, 16891–16903 (2014)
40. W.F. Beyer, I. Fridovich, Assaying for superoxide-dismutase activity: some large consequences of minor changes in conditions. *Anal. Biochem.* **161**, 559–566 (1987)
41. E. Peralta, G. Roa, J.A. Hernandez-Servin, R. Romero, P. Balderas, R. Natividad, Hydroxyl radicals quantification by UV spectrophotometry. *Electrochim. Acta* **129**, 137–141 (2014)
42. Y. Xu, M.A.A. Schoonen, The absolute energy positions of conduction and valence bands of selected semiconducting minerals. *Am. Miner.* **85**, 543–556 (2000)